Scaling and numerical analysis of non-isothermal sloshing for space propulsion

Pedro Afonso Duque Morgado Marques
pedro.morgado.marques@tecnico.ulisboa.pt

Instituto Superior Técnico, Universidade de Lisboa, Portugal

October 2020

Abstract

The motion of liquids inside a reservoir is called sloshing. This phenomenon is of interest to the aerospace industry given the prevalence of liquid-based propulsion systems in modern spacecraft. The fluid displacement generates destabilizing forces and moments which must be compensated by the attitude control systems. Moreover, when cryogenic fluids are considered, their high thermal sensitivities coupled with the liquid motion causes thermal mixing to take place between the gas and liquid phases. For critical conditions, large pressure fluctuations are observed, and the structural stability of the tank can be compromised. The aim of this work was to study the scaling laws of non-isothermal sloshing and investigate whether a small-scale laboratory model can reproduce the phenomena observed in the cryogenic stages of modern launch vehicles. This was done through Computational Fluid Dynamics simulations with OpenFOAM. The damping rates, interface position, sloshing forces and moments were analysed and similarity in the motion was compared between both facilities. The thermal destratification problem was studied for different initial thermal fields, different sloshing excitations and different thermal responses of the solid container walls. For planar sloshing conditions, the scaling approach yielded good similarity in terms of the flow dynamics as well as the thermodynamic evolution of the system. While the full-size facility was found to be less affected by the presence of wall-normal heat fluxes, the small-scale model was significantly impacted by this, leading to differences in the pressure and thermal evolutions of the systems.
Keywords: Sloshing, cryogenic fluids, pressure-drop effect, thermal destratification, CFD, OpenFOAM

1. Introduction

Liquid sloshing can be defined as the movement of the free liquid surface in a container or reservoir when subjected to a disturbance. This motion is associated with the displacement of a certain "sloshing mass" that produces forces and moments on the container's walls. These disturbances may be vibrations, acceleration changes, and pitch, roll or yaw motions. This phenomenon is of particular interest to the aerospace industry given the abundance of spacecraft which use liquid-based propulsion systems.

The focus of this work is on the cryogenic liquid propulsion systems, which are used in the upper stages of many modern launch vehicles, such as the Ariane 5-ECA (European Space Agency), Delta IV (United States), Long March 5 (China), and the H-IIB (Japan). These launchers use a combination of liquid hydrogen (LH_2) as propellant and liquid oxygen (LOx) as the oxidizer. During the initial propelled flight phase, as the launchers fly through the atmosphere, lateral sloshing has been detected inside the cryogenic stages [1]. The cryogenic tanks can be full up to 95% [2], and the resulting fluid displacement generates destabilizing forces and moments, which must be counteracted by the attitude control system.

Prior to launch, the cryogenic containers are pressurized up to 3.1-3.3 bar [3]. Due to the high thermal sensitivity of cryogenic fluids, this pressurization leads to the increase of the gas temperature in the tank. Then, as the system evolves towards thermal equilibrium, the warmer gas exchanges heat with the colder liquid propellant leading to a thermally stratified field in the container. Due to sloshing the stratified field is disturbed leading to thermal mixing between gas and liquid phases. As a result of this, the gas region cools down, decreasing its density. Consequently, the gas mass is no longer enough to maintain the current tank pressure, so this quantity must also decrease. This effect is accentuated by condensation effects at the interface [2]. This phenomenon is often referred to, in the literature, as the 'pressure drop effect', and it has been observed to take place in several flights of the Ariane 4 and 5 launchers [4]. The magnitude of this

drop depends on a series of factors, and it may cause several unwanted effects such as compromising the structural integrity of the propellant tank [2], and affecting the performance of cold gas thrusters, if they are used [5].

The presence of external heat fluxes (due to radiation, or thermal conduction within the rocket structure) must also be considered. These fluxes cause the fluids to warm up, and liquid evaporation to take place at the contact line [6]. In isolation, these effects are associated with an increase in the tank pressure. However, if liquid sloshing is also present both effects must be accounted for in order to accurately determine the thermodynamic evolution of the system.

The goal of this work is to analyse the scaling laws of non-isothermal sloshing and investigate whether a small scale laboratory model is capable of reproducing the main phenomena encountered in a full-size cryogenic tank. The analysis is carried out through CFD (Computational Fluid Dynamics) simulations with OpenFOAM. The focus is on understanding the role of lateral sloshing in the thermal destratification process, and the direct effect that this has in the pressure evolution. Therefore, no phase change effects are considered in the computational models.

The numerical study is carried out in two separate phases. First, the isothermal sloshing case is analysed in order to assess the scaling of the wave response between both facilities. The interface displacement, sloshing forces and moments are analysed in both the time and frequency domains, and numerical estimates are given for the damping rate of the systems. Then, the non-isothermal effects are studied in two different stages. First, the thermal stratification problem is assessed, then the non-isothermal sloshing simulations are performed in order to evaluate the similarity of the thermal mixing process in the full-size H_2 facility and in N_2 sloshing cell.

2. Theoretical background

Free surface oscillations in cylindrical containers can be considered as standing waves between two walls. For a container with radius R, filled with liquid at height h, subjected to a lateral harmonic excitation, the natural frequencies of the linear sloshing problem are given by Equation 1 [7].

$$\omega_{mn}^2 = \left(\frac{g\xi_{mn}}{R} + \frac{\sigma}{\rho}\frac{\xi_{mn}^3}{R^3}\right)\tanh\left(\frac{\xi_{mn}h}{R}\right) \qquad (1)$$

Where m, n are parameters that define the sloshing mode, ξ_{mn} is the n^{th} zero of the first derivative of the m^{th} order Bessel function (i.e. $J_m^{'}(\xi_{mn}) = 0$), and σ is the surface tension. The lowest wave mode that can be excited in lateral sloshing conditions is the first asymmetrical one $m = n = 1$. This mode is characterized as an approximately flat wave that moves with the direction of excitation. Observations on the initial propelled phase of launch vehicle flights show that this $(1, 1)$ mode is the primary fluid response in cryogenic stages as the spacecraft ascends through the atmosphere [2, 8]. As such, the focus of this work is on excitations close to this natural frequency, ω_{11}.

According to Miles' weakly nonlinear theory [9], the fluid response to a forced oscillatory lateral motion is directly dependent on the excitation parameters, namely the imposed amplitude A_0, and frequency Ω of the movement. Three different wave responses may be observed, depending on the selection of these two parameters: planar waves, chaotic sloshing, swirl waves. For lateral sloshing excitations, near ω_{11}, Miles determined that the boundaries between these regimes are defined by Equation 2, where $\mathfrak{B}_i$ are the fixed values of the frequency offset parameter that separate the different sloshing regimes: $\mathfrak{B}_2 = -0.36$, $\mathfrak{B}_3 = -1.55$, and $\mathfrak{B}_4 = 0.735$.

$$\frac{A_0}{R} = \frac{1}{1.684}\left(\frac{(\Omega/\omega_{11})^2 - 1}{\mathfrak{B}_i}\right)^{3/2} \qquad (2)$$

Figure 1 shows the phase diagram for the different sloshing regimes that can be obtained by varying the dimensionless excitation amplitude A_0/R and frequency Ω/ω_{11}.

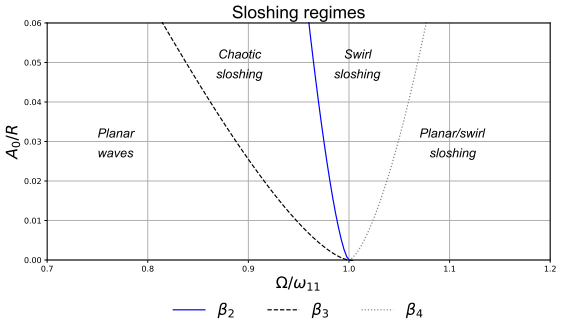

Figure 1: Phase diagram for the different sloshing regimes.

For planar waves conditions, the wave response is given by the superposition of the steady-state response to the forced oscillation with the initial transient solution, excited at the natural frequency, which is gradually damped over time [2]. The damping rate of the system, γ, due to viscous dissipation of the flow on the container walls and interface, is estimated by the empirical correlation presented in Equation 3, where ν is the liquid's kinematic viscosity, and C_1, n_1 are parameters depen-

dent on the problem's geometry. For a cylindrical container without baffles, $C_1 = 0.79$, $n_1 = 1/2$ [10].

$$\gamma = C_1 \left(\frac{\nu}{R^{3/2} g^{1/2}}\right)^{n_1} \left(1 + \frac{0.318}{\sinh(\xi_{1n} h/R)} \left(1 + \frac{1 - h/R}{\cosh(\xi_{1n} h/R)}\right)\right) \tag{3}$$

3. Problem setup

The small-scale facility considered in this work is the VKI (von Karman Institute) sloshing cell. This consists of a quartz cylindrical container with flat top and bottom, with 40 mm radius and total height 104 mm. The large-scale facility is obtained by scaling up the small-scale model by a factor of fifty. This results in a cylindrical sloshing tank with radius 2000 mm, and total height 5200 mm. These dimensions are in agreement with typical full-size cryogenic containers found in the literature [1, 11, 12]. The setup for this study is summarized in Table 1.

Table 1: Dimensions for the full-size cryogenic tank and the small-scale laboratorial model

	R (m)	H (m)	Fill level (%)
Sloshing cell	0.04	0.104	80
Full-size tank	2	5.2	

4. Scaling analysis

4.1. Governing equations and boundary conditions

The dimensionless numbers that control the flow are obtained by scaling the governing equations and relevant boundary conditions of the non-isothermal sloshing problem. The main assumption for the scaling approach followed in this work is that the main driver for the thermodynamic evolution of the system is the mixing that takes place between the interface and the sub-cooled liquid region underneath it [2]. As a result, the dimensionless numbers are generated by scaling the equations and boundary conditions which govern the liquid phase. This includes the typical three conservation laws of mass (Equation 4), momentum (Equation 5) and thermal energy (Equation 6) in incompressible form. The Boussinesq approximation is introduced in the buoyancy term of the momentum balance in order to account for thermally-induced density variations in the fluid [2].

$$\nabla \cdot \mathbf{u} = 0 \tag{4}$$

$$\rho_0 \frac{\partial \mathbf{u}}{\partial t} + \rho_0 \mathbf{u}(\nabla \cdot \mathbf{u}) = -\nabla p + \mu \nabla^2 \mathbf{u} + \rho_0 (1 - \beta \Delta T)\mathbf{g} \tag{5}$$

$$\rho_0 C_v \left(\frac{\partial T}{\partial t} + \mathbf{u} \cdot \nabla T\right) = k \nabla^2 T \tag{6}$$

The no-slip boundary condition is considered with respected to the solid walls. The Young-Laplace equation is used to model the stresses applied at the liquid-gas interface, by balancing the pressure difference between both phases with surface tension σ and the free surface curvature κ [13].

$$\Delta p = p_{\text{liq}} - p_{\text{gas}} = -\sigma\kappa. \tag{7}$$

Since the free-surface is the separation point between the gas and liquid phases, this region is considered to be at saturation conditions, $T_{\text{i}} = T_{\text{sat}}$ [2]. Thus, using the Clausius-Clapeyron law [4], the pressure of the vapour phase is directly related to the temperature of the interface:

$$\ln\left(\frac{p}{p_0}\right) = \frac{\Delta h_v}{R_s}\left(\frac{1}{T_{\text{sat},0}} - \frac{1}{T_{\text{sat}}}.\right). \tag{8}$$

If the interface cools down, the saturation temperature decreases, which means that, in order to remain in equilibrium conditions, condensation of the vapour phase must take place to reduce the pressure. The reverse mechanism is observed when the temperature of the interface increases. Therefore, even if phase change effects are not directly modeled in the computational approach, a qualitative assessment on the presence of evaporation or condensation can still be made by monitoring the temperature of the free surface during the non-isothermal sloshing simulations.

4.2. Dimensionless numbers

Table 2 contains the list of reference quantities used for the nondimensionalization Equations 4, 5, 6 and 7. The complete set of the obtained dimensionless numbers is shown in Table 3.

Table 2: Reference parameters considered for the scaling analysis.

Physical parameter	**Reference**	**Definition**
Length	R	Tank radius
Velocity	$A_0\Omega$	Excitation velocity
Time	$R/A_0\Omega$	Length/Velocity
Pressure	$\rho_0(A_0\Omega)^2$	Dynamic pressure
$[\Delta T_{\text{ref}}]$	$T_{\text{gas}} - T_{\text{liq}}$	Warm - Cold

The Reynolds number (Re) relates the relative strength of viscous forces when compared to inertial ones. This parameter is crucial in sloshing applications since it offers an estimate for the damping that the liquid experiences as it moves along the container walls [7]. The Froude (Fr) and Weber (We) numbers compare the relative strength of hydrodynamic forces, thus determining which hydrodynamic regime may be expected (i.e.

Table 3: Dimensionless numbers for the nonisothermal lateral sloshing problem

	DN	Expression
π_1	Re	$\frac{\rho_0(A_0\Omega)R}{\mu}$
π_2	Fr	$\frac{A_0^2\Omega^2}{gR}$
π_3	$\frac{\mathrm{Gr}}{\mathrm{Re}^2}$	$\frac{gR\beta\Delta T_{ref}}{A_0^2\Omega^2}$
π_4	Pe	$\frac{\rho_0 C_v(A_0\Omega)R}{k}$
π_5	We	$\frac{\rho_0(A_0^2\Omega^2)R}{\sigma}$

gravity-dominated, capillary-dominated, inertia-dominated). Buoyancy driven convection is related to inertial forces through the π_3 parameter. Finally, the ratio of thermal diffusion to advection is related to the Peclet number (Pe).

4.3. Scaling approach

Kinematic similarity of the sloshing problem is achieved by guaranteeing that the frequency offset parameter $\mathfrak{B}$, is the same for both the small-scale model and the full-size facility [**?**]:

$$\mathfrak{B} = \frac{\left(\frac{\Omega}{\omega_{11}}\right)^2 - 1}{\left(1.684\frac{A_0}{R}\right)^{2/3}}. \tag{9}$$

If the dimensionless excitation parameters, Ω/ω_{11} and A_0/R, are constant between both facilities, the frequency offset parameter is enforced and similar wave responses are observed.

Dynamic similarity is assured if all dimensionless numbers are equal for both the small-scale model and the large cryogenic tank. Imposing the dimensionless excitation parameters for both facilities allows for equality to be maintained in terms of the Froude number. This guarantees that the relative importance of inertia and volume forces in the flow is the same.

The Reynolds, Peclet and Webber numbers are exclusively dependent on the tank dimensions and on the fluid's properties. As a result, given that the container dimensions are imposed on the problem, similarity with respect to these quantities can only be attempted through the adequate choice of fluid for the small-scale model. This raises several difficulties since there is no known fluid which can lead to perfect matching of the dimensionless numbers in both sloshing facilities. The full size facility is filled with cryogenic H_2, and the small-scale model is typically operated with engineering fluids (HFE7000, HFE7200) or cryogenic N_2 [2, 5].

Figures 2, 3 4 show the similarity in terms of the Reynolds, Peclet and Weber numbers for both facilities considering N_2, HFE7000 and HFE7200 as replacement fluids for H_2, and assuming a linear

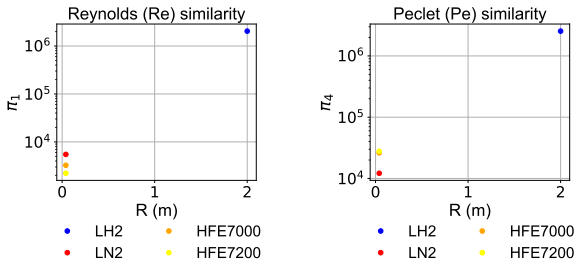

Figure 2: π_1 similarity.

Figure 3: π_4 similarity.

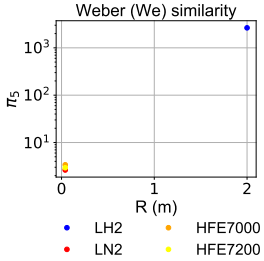

Figure 4: π_5 similarity.

sloshing excitation with $A_0/R = 0.045$ and $\Omega/\omega_{11} = 0.7$. When comparing the dimensionless numbers for the full-size and small-scale cases, a difference of 2 to 3 orders of magnitude can be observed for the chosen replacement fluids. This is attributed to the large differences in scale between both tanks.

On the other hand, π_3 is additionally dependent on the reference temperature difference ΔT_{ref}. Thus, similarity for this parameters is improved by imposing adequate values for the initial thermal field in the sloshing containers. This is achieved through a simplified approach for the modeling of the thermal stratification process. An initial state is set for the container, where both the gas and liquid regions are assumed to have constant temperature, equal to T_{gas} and T_{liq}, respectively. Then, the system is allowed to progress towards equilibrium with heat transfer taking place between the warmer gas and the colder liquid. This leads to the formation of the characteristic thermally stratified field.

The temperature of the gas and liquid is known for the full-size H_2 facility from the master's thesis of Hoppe (2013) [3]. The average temperature of the gas is 47.3 K and the liquid is at 20.6 K. Table 4 shows the required values for the temperature difference between the gas and liquid regions in order guarantee perfect similarity in terms of the liquid-based π_3 parameter. These results highlight the difficulty of using non-cryogenic fluids for the current non-isothermal analysis given the impractically large ΔT required by this scaling approach. Consequently, cryogenic N_2 was considered as the replacement fluid for H_2 in the numerical analysis.

Table 4: Temperature information for H_2 and the replacement fluids in order to guarantee perfect similarity in terms of the π_3 dimensionless parameter.

	H_2	N_2	HFE7200	HFE7000
ΔT(K)	26.7	77.65	271.83	218.91
T_{liq}(K)	20.6	77.35	-	-
T_{gas}(K)	47.3	155	-	-

5. Numerical methods

5.1. Volume of Fluid method

The Volume of Fluid (VOF) method [14] is employed in order to track the liquid and gas phases alongside their interface in the computational domain. A single set of conservation equations are solved alongside the advection equation for the volumetric phase fraction α_f:

$$\frac{\partial \alpha_f}{\partial t} + \nabla \cdot (\alpha_f \mathbf{u}) = 0. \tag{10}$$

If $\alpha_f = 1$, the cell is fully filled with fluid f, whereas if $\alpha_f = 0$ there is none. Cells which contain α_f values between 0 and 1 indicate the presence of the interface. After the determination of the α_f field, equivalent fluid properties are computed in each cell based on the individual fluid properties and on the volume fraction field.

5.2. Isothermal sloshing

The isothermal simulations were conducted with the `interFoam` solver. This is a two-phase solver for immiscible, incompressible and isothermal fluids that solves a single set of continuity and momentum equations alongside the α advection equation [15].

In order to give stability to the solution and to simplify the definition of boundary conditions, the pressure is treated through the `p_rgh` variable [15]:

$$p_{rgh} = p - \rho \mathbf{g} \cdot \mathbf{x}. \tag{11}$$

An additional source term is also added to the momentum equation in order to account for capillary forces near the interface. This is achieved through the Continuum Surface Model (CSF) developed by Brackbill *et. al* (1992) [16]. The interface is captured by solving the volumetric phase fraction advection equation with an additional compression term that aims to reduce numerical diffusion and smearing of the interface [17].

5.3. Non-isothermal sloshing

In order to model the non-isothermal effects and pressure fluctuations that take place inside the cryogenic containers, the pressure-based `compressibleInterDyMFoam` solver was considered. This is a variation of the `interFoam` solver which is aimed at compressible flow problems and solves the energy balance alongside the momentum, continuity and α advection equations.

The solver allows for different thermophysical models to be considered for the two phases. Thus, the Boussinesq approximation was used for the liquid phase, and the ullage gas was treated with the ideal gas model. This approach was used in the works of Himeno (2011) [18], Agui (2015) [19], and Kartuzova (2018) [20]. However, unlike those cases, mass transfer effects are not considered in this work since the focus is to study the impact of sloshing on the thermal de-stratification effect. The numerical simulations presented in this work allow for the decoupling of the momentum and energy exchanges from the mass transfer effects, which is not possible for real life experimental conditions.

5.4. Numerical grid and schemes

The three-dimensional numerical grid was generated using the `blockMesh` utility included with the installation of `OpenFOAM-v1912`. A total of 36 regions (or blocks) were generated in order to adequately model the cylindrical container.

The chosen temporal scheme was the first-order implicit Euler, the gradient and laplacian terms were discretized with second-order Gauss linear, and the divergence terms were treated with the second-order TVD (Total Variation Diminishing) flux-limiting van Leer scheme. The fluid properties for the numerical simulations were obtained from the NIST database [21].

6. Isothermal results

The isothermal sloshing simulations were performed in the planar waves regime with dimensionless excitation parameters $\Omega/\omega_{11} = 0.7$ and $A_0/R = 0.045$. The dimensionless interface displacement η^*, lateral force F_x^* and moment M_y^* (with respect to the bottom of the container) are sampled for the full-size H_2 facility and the N_2 sloshing cell. The non-dimensionalization of these flow parameters is based on the reference quantities used to scale the governing equations as shown in Equation 12.

$$\eta^* = \frac{\eta}{R} \quad ; F_x^* = \frac{F_x}{\rho_0 (X_0 \Omega)^2 R h} \quad ; M_y^* = \frac{M_y}{\rho_0 (X_0 \Omega)^2 R h^2} \tag{12}$$

Figure 5 shows the initial transient force response that occurs when the excitation is applied directly from rest. The Discrete Fourier Transform (DFT) of these signals (Figure 6) indicates that this motion is the superposition of two waves operating at different frequencies: ω_{11} and Ω.

The natural frequency contribution is damped due to viscous dissipation both at the container walls and the interface, resulting in the harmonic motion found in Figures 7 and 8. These results

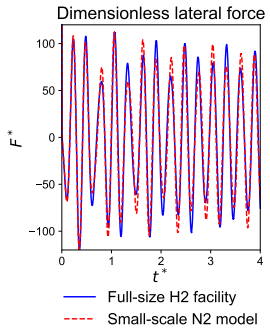

Figure 5: F_x^* in both facilities between $t^* = 0$ and $t^* = 4$.

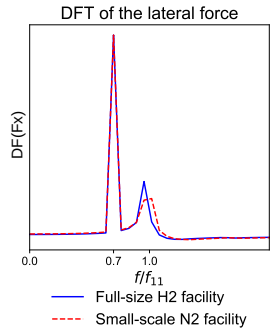

Figure 6: DFT of F_x^* in both facilities between $t^* = 0$ and $t^* = 4$.

show good similarity in the numerical simulations of both sloshing containers, especially when the stable sloshing regime is reached. For these conditions, the small-scale results can be scaled up in order to predict the flow response in the large container with great accuracy. This is also true for the dimensionless interface displacement and lateral sloshing moment.

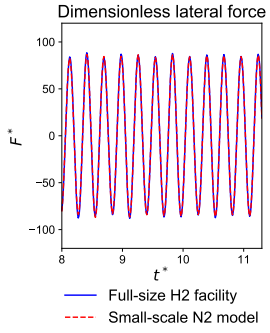

Figure 7: F_x^* in both facilities between $t^* = 8$ and $t^* = 11.2$.

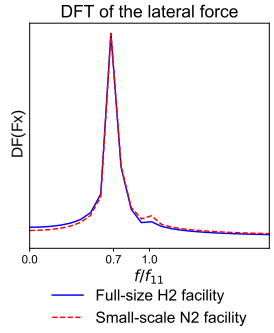

Figure 8: DFT of F_x^* in both facilities between $t^* = 8$ and $t^* = 11.2$.

During the transient period, higher-frequency wave modes are excited and gradually damped. This means that differences in the damping ratio of the system lead not only to distinct flow responses during this stage, but also to different durations of the transient state itself in both containers.

The theoretical damping rates for both systems are estimated by Equation 3 as $\gamma_{\mathrm{H2_{theor}}} = 1.14E-4$ and $\gamma_{\mathrm{N2_{theor}}} = 2.21E-3$. However, the numerical estimates for this parameter are considerably higher, with $\gamma_{\mathrm{H2_{num}}} = 0.0102$ and $\gamma_{\mathrm{N2_{num}}} = 0.011$. It is believed that numerical diffusion dominates the problem and because of this, $\gamma_{\mathrm{H2_{num}}}$ and $\gamma_{\mathrm{N2_{num}}}$ are not accurate measures for the real damping in the system.

Grid refinement studies on this problem revealed that the numerical damping rate of this system decreased when increasing both the spatial and temporal resolutions of the numerical discretization. However, the computational resources required to achieve the theoretical damping rates in the numerical discretization were too demanding for the current study. These changes affected only the initial transient regime, and once the higher frequency contribution was damped, the steady harmonic motion was identical for all the tested numerical grids.

As a result, while one should be very critical of the fluid response observed during the initial transient period, the the similarity observed in the steady harmonic regime is still valid.

7. Non-isothermal results

The non-isothermal analysis is decomposed in two steps. First, the thermal stratification problem is assessed and thermally stratified fields are generated for both the full-size and small-scale facilities. Then, utilizing these fields inputs, the non-isothermal sloshing simulations are performed in order to evaluate the similarity of the thermal destratification process.

7.1. Thermal stratification

Thermal stratification simulations were performed in both the H_2 and N_2 facilities, assuming an initial state where both the gas and the liquid regions have uniform temperatures, T_{gas} and T_{liq}, respectively (refer to Table 4) (Figure 9). Then, the system is allowed to progress towards equilibrium with heat transfer taking place between the gas and liquid phases.

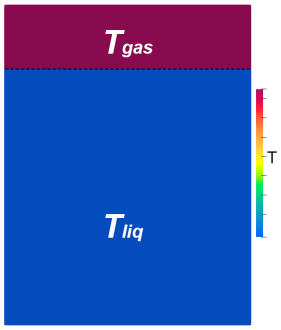

Figure 9: Initial state assumed for the gas and liquid phases.

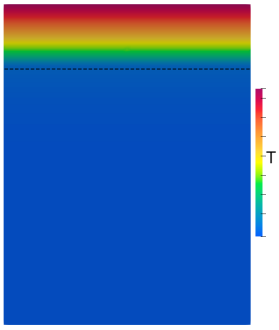

Figure 10: Thermally-stratified field used as input for sloshing.

Fixed temperature boundary conditions were used for the top and bottom faces, whereas the lateral walls were considered to be adiabatic. The top face was considered to be at temperature T_{gas} and the bottom T_{liq}. The stopping point for these simulations was based on the Fourier number of the liquid phase:

$$\mathrm{Fo}_{\mathrm{liq}} = \frac{\alpha_{\mathrm{liq}} t}{h^2}. \tag{13}$$

Where h is the liquid height inside the container. The temperature fields were found to evolve from the initial conditions much faster in the small-scale model compared to the full-size scenario. Therefore, three distinct thermal fields were generated in this step, and later used as inputs for the thermal mixing simulations:

1. H_2, with $\mathrm{Fo}_{\mathrm{liq}} = 7.16E-5$ and t = 1200s
2. N_2, with $\mathrm{Fo}_{\mathrm{liq}} = 7.16E-5$ and t = 1.35s
3. N_2, with $\mathrm{Fo}_{\mathrm{liq}} = 2.54E-4$ and t = 460s

Thermal fields 1 and 2 were generated for the full-size facility and small-scale model, respectively, for the same liquid-based Fourier number. Since the thermal-field in the small-scale model was still changing very quickly for this instant, thermal field 3 was generated for a more stable point in time, as can be seen in Figures 11 and 12. The purpose of this additional case is to check the effect that a more developed thermal field has on destratification process.

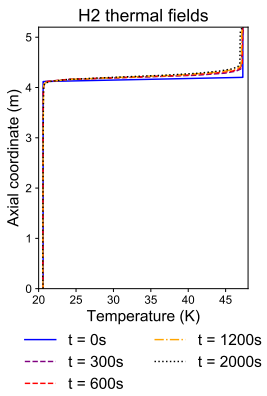

Figure 11: Evolution of the thermal fields in the full-size H_2 facility.

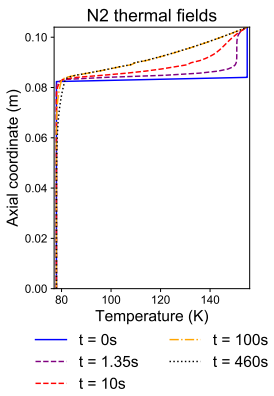

Figure 12: Evolution of the thermal fields in the full-size H_2 facility.

Figures 13 and 14 show the dimensionless thermal profiles for H_2 and N_2 in both the liquid and gas phases. Fields 1 and 2 show good similarity for the temperature distribution when using the same liquid-based Fourier number.

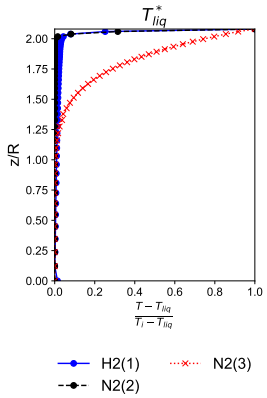

Figure 13: Dimensionless thermal fields in the liquid.

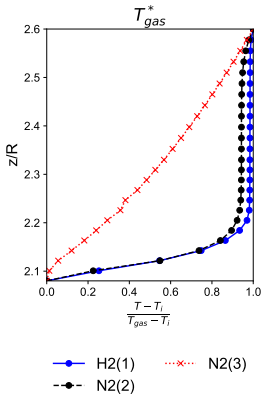

Figure 14: Dimensionless thermal fields in the gas.

7.2. Thermal mixing

The thermal mixing simulations were performed using the thermally stratified fields, obtained in the previous section, as the initial conditions. Since the solid container walls are not modeled in the numerical approach of the non-isothermal problem, the effect of different wall boundary conditions is assessed in two different configurations.

The two test cases are defined as A and B, and they model two extreme situations for the thermal response of the lateral walls. Case A considers the lateral walls to be adiabatic, while case B assumes that these are at fixed temperatures. The portion originally in contact with the gas is fixed at T_{gas}, whereas the liquid region is at T_{liq}. In both cases, the upper and the bottom tank walls are assumed to remain at uniform temperature T_{gas} and T_{liq} respectively.

Simulations were performed in the planar waves regime, with dimensionless excitation parameters: $\Omega/\omega_{11} = 0.7$, $A_0/R = 0.045$. For this case, similarity between the H_2 and N_2 facilities was assessed while studying the:

1. Effect of the wall boundary conditions, comparing configuration A with configuration B
2. Effect of the duration of the thermal stratification, through the comparison of the different thermally stratified fields as initial conditions for the thermal mixing simulations

7.3. Effect of the wall boundary conditions

Thermal fields 1 and 2 were considered for this analysis. The average dimensionless temperature of the interface given by:

$$T_{\mathrm{i}}^{*} = \frac{T_{\mathrm{i}} - T_{\mathrm{liq}}}{T_{\mathrm{gas}} - T_{\mathrm{liq}}} \tag{14}$$

was monitored throughout the simulation, and its evolution is plotted alongside the dimensionless time $t^{*} = tA_0\Omega/R$ in Figure 15.

Cases H2(A) and H2(B) are characterized by an overall decrease in interface temperature, which slows down as the time thermal field approaches equilibrium. Case N2(A) presents a very sharp initial temperature drop until $t^* \approx 0.1$, then it increases slightly until $t^* \approx 0.76$, and afterwards, a very gradual decrease is observed until the end of the simulation. On the other hand, case N2(B) presents a behaviour that is very different from all other tested situations. For this situation, there is an initial sharp drop until $t^* = 0.08$, which is followed by a progressive increase of T_i^* until the the end.

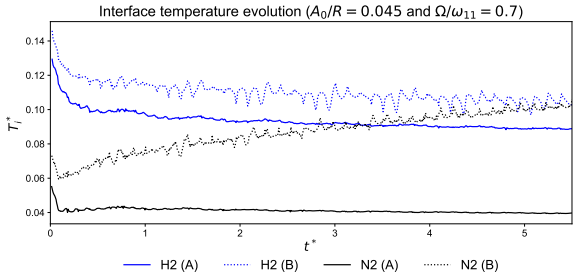

Figure 15: Dimensionless interface temperature evolution for the H_2 and N_2 containers in planar sloshing conditions.

These diverging results for the evolution of the interface temperature in case N2(B) are problematic because the interface is considered to be at saturation conditions $T_{sat} = T_\mathrm{i}$. Following the Clausius-Clapeyron law (Equation 8), the saturation temperature of the system directly affects the pressure of the vapour phase, which means that a decrease in T_{sat} causes a decrease in p_{vap} and *vice-versa*. This means that for configuration N2(B), this mechanism is not working accordingly to what was expected from the full-size facility results. Therefore, condensation and evaporation effects would likely differ significantly between the full-size and scaled-down facilities if they were taken into account in this analysis.

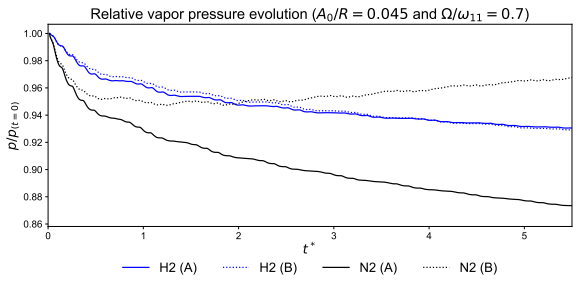

Figure 16: Relative tank pressure evolution for the H_2 and N_2 containers, in planar waves conditions, with different wall boundary conditions applied.

The relative pressure drop p/p_0, where p_0 is the initial tank pressure prior to sloshing is shown in Figure 16. The behaviour shown in this plot is in agreement with the observations made regarding the T_i^* evolution. Cases H2(A), H2(B) and N2(A) all show an overall decrease in T_i^* and p/p_0 during this simulation. This suggests that the sloshing-induced thermal mixing promotes a general cooling down of the ullage due to the presence of the colder liquid. As a result, these three cases are all characterized by a steady pressure drop. The biggest decrease in pressure takes place in the N2(B) facility (87% of the initial value).

On the other hand, case N2(B) shows an overall increase in T_i^* as well as p/p_0 during the simulation. This case models the extreme scenario in which the portion of the side-walls initially in contact with the gas (top 20%) has fixed temperature T_gas, and the remaining portion (bottom 80%) is at T_liq. These results suggest that, for the current excitation conditions, the presence of the warmer walls overcomes the sloshing-induced thermal mixing, causing an increase in the ullage temperature. This is the opposite of what is expected from the full-size facility results.

The greater sensitivity of the smaller domain to the presence of the heated walls could be linked to the difference in the Peclet number between both facilities. The N_2 sloshing cell has a Peclet number that is 2 orders of magnitude smaller than the full-size facility. This means that thermal diffusion effects should a greater role in case N2(B2) compared to H2(B), provided that the rates of advective transport are similar in both cases.

Figures 17 and 18 show the thermal fields and the gas-liquid interface for the N2(A) and N2(B) cases, respectively, for different time instants. The N2(A) sequence of images shows the gradual cooling down of the ullage due to the presence of the colder liquid. The thermal mixing that happens below the interface allows for the free surface to remain cold, while gradually exchanging heat with the gas to decrease its temperature. On the other hand, in case N2(B), the presence of the lateral and top walls at T_gas counteracts the cooling mechanism of the liquid, leading to a gradual increase in temperature from the top of the container to the bottom.

Figure 19 shows the velocity and the dimensionless temperature fields near the interface. The fluid in the downward side of the planar wave is pushed to the bottom of the container, where it is cooled down by the bulk, and the fluid in the upward side of the wave receives colder liquid from the bottom, thus decreasing its temperature. This is the mechanism responsible for the cooling down of the gas phase observed in cases H2(A), H2(B) and N2(A).

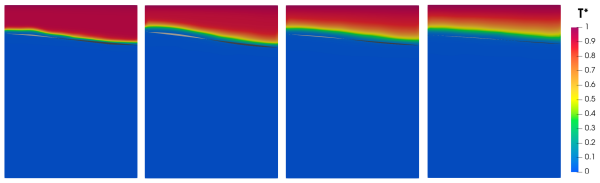

Figure 17: Dimensionless thermal fields and interface position for the planar N2(A) case at $t^* = 0.16$ (far left), $t^* = 1.23$ (center left), $t^* = 3.05$ (center right) and $t^* = 5.53$ (far right).

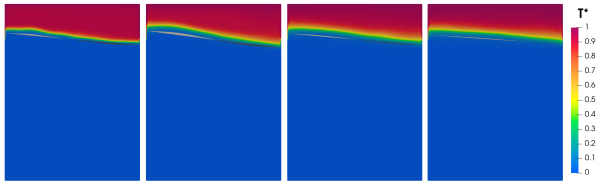

Figure 18: Dimensionless thermal fields and interface position for the planar N2(B) case at $t^* = 0.16$ (far left), $t^* = 1.23$ (center left), $t^* = 3.05$ (center right) and $t^* = 5.53$ (far right).

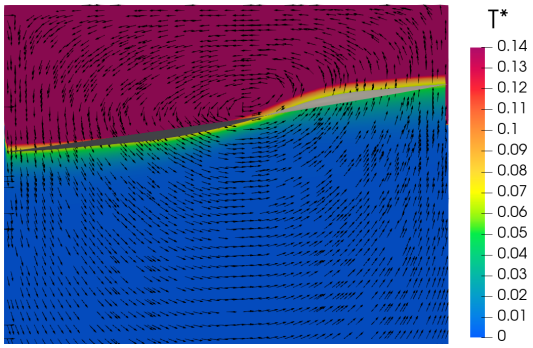

Figure 19: Sloshing velocity field and thermal mixing mechanism.

7.4. Effect of the thermal stratification duration

Thermal fields 2 and 3 are considered in this analysis in order to compare the effect of the initial thermal stratification on the non-isothermal sloshing problem. The wall boundary condition configuration selected for this analysis was case (B).

The dimensionless interface temperature for cases N2(B2) and N2(B3) is shown in Figure 20. The plot reveals that the more developed initial thermal field of case N2(B2) leads to a higher increase in T_i^* as time progresses. Moreover, from Figure 21, the relative tank pressure in this case doesn't show a drop at all. Instead the ratio p/p_0 increases since the start of the simulation.

Figure 22 shows the evolution of the dimensionless thermal fields and interface position as time progresses in the N2(B3) case. From these images, it is clear that, similarly to what happened in case N2(B2), the presence of the warmer walls at T_{gas}

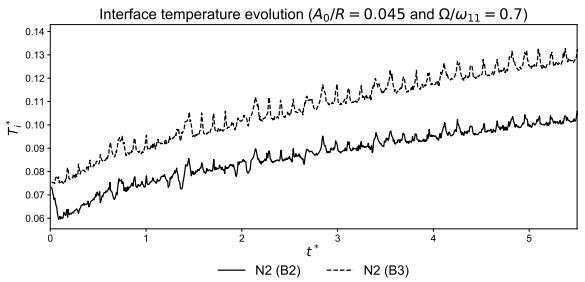

Figure 20: Dimensionless interface temperature evolution for the H_2 and N_2 containers in planar sloshing conditions for different durations of initial thermal stratification.

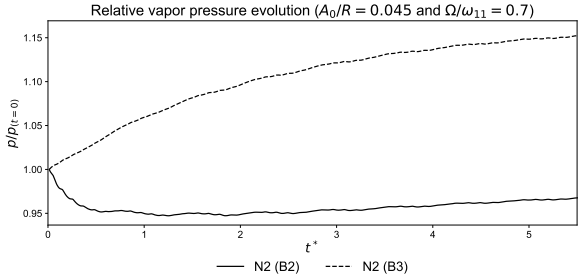

Figure 21: Relative tank pressure evolution for the H_2 and N_2 containers in planar sloshing conditions for different durations of initial thermal stratification.

overcomes the cooling effect of the thermal mixing below the interface. Moreover, since the initial thermal field started from a more developed situation, the thermal gradients near the interface are lower, which translates to a reduction of the mixing effect. As a result, the cooling of the ullage due to the liquid mixing is reduced, meaning that the heating effect of the warm walls is felt with more intensity.

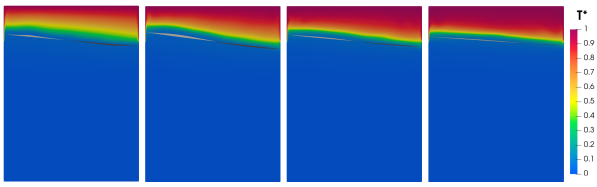

Figure 22: Dimensionless thermal fields and interface position for the planar N2(B2) case at $t^* = 0.16$ (far left), $t^* = 1.23$ (center left), $t^* = 3.05$ (center right) and $t^* = 5.53$ (far right).

8. Conclusions

The results of the isothermal simulations showed that good similarity was found for flow response between the full-size facility and the scaled-down model for the steady periodic regime in planar

sloshing. However, the initial transient state could not be truly compared between both cases due to the presence of excessive numerical discretization. A great deal of computational resources are required in order to spatially and temporally refine the numerical grids in order match the theoretical damping rates of the systems.

The results of the non-isothermal simulations showed that when adiabatic conditions are used for the container's side walls, the thermodynamic evolution of the system is similar between the full-size facility and the scaled-down model. Due to the sloshing-induced thermal mixing, the pressure decreased $\approx$ 6% in H2 tank and $\approx$ 12% in the N2 sloshing cell. For both these cases, a continuous cooling of the ullage was observed throughout the duration of the excitation. On the other hand, when the fixed temperature boundary conditions were used for the container side-walls, the small-scale facility showed a great sensitivity to the presence of the warm regions. For cases N2(B2) and N2(B3) the cooling down effect promoted by the sloshing motion was overcome by the heat coming off the walls. Thus, an increase in pressure was observed for these cases.

This work should be further developed by incorporating the effect of the solid walls and the gas into the scaling approach. Moreover, the computational modeling should be extended in order to account for conjugate heat transfer between the fluid phases, the solid walls and any exterior heat fluxes which might be present. Additionally, mass transfer effects between the liquid and the gas should be included in order to obtain a more complete comparison of the thermodynamic evolution of the system, namely the pressure drop.

References

[1] Michael Dreyer. Propellant behavior in launcher tanks: an overview of the compere program. *EUCASS Proceedings Series*, 1:253–266, 09 2009.

[2] Tim Arndt. *Sloshing of Cryogenic Liquids in a Cylindrical Tank under normal Gravity Conditions*. PhD thesis, Bremen Univseristy, 2011.

[3] Charlotte Hoppe. LH2 Tank performance analysis. *KTH Vetenskap och Konst*, 2013.

[4] Christophe Montsarrat. Fluid motion analysis in the cryogenic tanks of the upper stage of Ariane 5 during the ascent phase. *KTH Vetenskap och Konst*, 2017.

[5] Martin Konopka, Philipp Behruzi, Sebastian Schmitt, and Michael Dreyer. Phase change in cryogenic upper stage tanks. 07 2014.

[6] Sebastian Schmitt. *Experimental and Numerical Investigations of Two-Phase Flow with Non-Isothermal Boundary Conditions under Microgravity Conditions*. PhD thesis, Bremen University, 2017.

[7] Raouf A. Ibrahim. *Liquid sloshing dynamics*. 2005.

[8] Michael Dreyer. Propellant behavior in launcher tanks: an overview of the compere program. *EUCASS Proceedings Series*, 1:253–266, 09 2009.

[9] John W. Miles. Resonantly forced surface waves in a circular cylinder. *Journal of Fluid Mechanics*, 149:15–31, 1984.

[10] H. Norman Abramson, Franklin T. Dodge, Helmut F. Bauer, George W. Brooks, Wen-Hwa Chu, John F. Dalzell, Daniel D. Kana, William C. Reynolds, Hugh M. Satterlee, and Sandor Silverman. *The Dynamic Behavior of Liquids in Moving Containers*. NASA, 1966.

[11] Zhan Liu, Yuyang Feng, Gang Lei, and Yanzhong Li. Fluid thermal stratification in a non-isothermal liquid hydrogen tank under sloshing excitation. *International Journal of Hydrogen Energy*, 43(50):22622–22635, 2018.

[12] Arianespace. Ariane 5 User's Manual. (5 Revision 2), 2016.

[13] Michael E. Dreyer. *Free Surface Flows under Compensated Gravity Conditions*, volume 221. Springer, Bremen, 2003.

[14] C.W Hirt and B.D Nichols. Volume of fluid (vof) method for the dynamics of free boundaries. *Journal of Computational Physics*, 39(1):201 – 225, 1981.

[15] Santiago Márquez Damiáno. An extended mixture model for the simultaneous treatment of small-scale and large-scale interfaces. *International Journal for Numerical Methods in Fluids*, (75):547–574, 2014.

[16] J.U Brackbill, D.B Kothe, and C Zemach. A continuum method for modeling surface tension. *Journal of Computational Physics*, 100(2):335 – 354, 1992.

[17] Henrik Rusche. Computational Dispersed Two-Phase Dynamics Flows of At Phase Fractions. (December 2002), 2003.

[18] Takehiro Himeno, Daizo Sugimori, Katsutoshi Ishikawa, and Yutaka Umemura. Heat Exchange and Pressure Drop Enhanced by Sloshing. pages 1–40, 2011.

[19] Juan Agui and Jeffrey Moder. Modeling of non-isothermal cryogenic fluid sloshing. 07 2015.

[20] O. Kartuzova and M. Kassemi. Validation of a Cfd Model Predicting the Effect of High Level Pressure Drop in a Small-Scale Tank in Normal Gravity. pages 1–21, 2018.

[21] Siderius D.W. Krekelberg W.P. Shen, V.K. and H.W. Hatch. *NIST Standard Reference Database Number 173, National Institute of Standards and Technology, Gaithersburg MD, 20899*, volume 3. NIST Standard Reference Simulation Website, Retrieved: 2020-05-21.